Supplementary Information (SI) for Energy & Environmental Science.
This journal is © The Royal Society of Chemistry 2025

Supplemental Information

Regulating segmental dynamics for ion-cluster in polymer binder to realize high-areal-capacity electrodes in lithium batteries

Dong-Yeob Han‡[a], Sungryong Kim‡[b], Yeongseok Kim[a], Haeryang Lim[b], Gyeong Rok Lee[d], Chi Keung Song[e], Woo-Jin Song[e], Hong Chul Moon*[c], Soojin Park*[a], and Taiho Park*[b]

Contents

Supplemental experimental procedures

Figure and Table legends

Note 1. The synthesis of the polymers.

Fig. S1. ^{1}H NMR, ^{7}Li NMR, and ^{13}C NMR spectra of lithium sulfopropyl-methacrylate (LSP), ^{1}H NMR and ^{13}C NMR spectroscopy of methacryloyl 3,4-dihydroxyl-L-phenylalanine (DOPA), and ^{1}H NMR spectra of the ISP0, ISP33, ISP50, ISP67, and ISP100.

Fig. S2. GPC profiles in the ISP series.

Fig. S3. Solubility of the ISP series in NMP.

Fig. S4. Temperature-dependent behavior in the ISP series by DSC.

Fig. S5. The FT-IR spectra of a) the ISP series in the film state, and b) comparison of ISP33, ISP50, and ISP67 in solution and film state. c) Relative peak shift between solution and film state in ISP33, ISP50, and ISP67.

Fig. S6. a-c) The FT-IR spectra and d) relative peak shift of the ISP33, ISP50, and ISP67 films depending on the temperature

Fig. S7. a) Diagram of the polymer chain behavior (Tan δ) depending on the frequencies. b) The tan δ of the ISP series under angular frequencies.

Fig. S8. The complex viscosity and storage compliance of the ISP series under angular frequencies.

Fig. S9. The tensile S-S curve depending on the time (quantitative self-healing), along with inset OM images (qualitative self-healing) of the a) ISP0, b) ISP33, and c) ISP67.

Fig. S10. Bode plots of the ISP series and PVDF depending on the polarization, ion migration, and electrical double layer (EDL) regions.

Fig. S11. a-d) Real and imaginary impedance depending on the frequencies, and e-h) relaxation time of the ISP series at the various temperatures.

Fig. S12. a) Charge and b) dielectric relaxation time of mobile ions in the ISP series at -40 °C condition.

Fig. S13. Resistance change of the ISP series a) under several stretching conditions and b) under repeated 100% stretching condition.

Fig. S14. Schematic illustration of the SAICAS process.

Fig. S15. Electrochemical floating analysis of the NCM811 cathodes.

Fig. S16. Galvanostatic charge-discharge profiles of the ISP50 and PVDF cathodes.

Fig S17. a) Discharge rate capability and b) long-term cycling performance of NCM811 cathodes with different ISP binders.

Fig. S18. a) GITT profiles obtained upon the repeated current stimuli at 0.5 C. b) Average internal resistance and Li^{+} diffusion coefficient values of cathodes.

Fig. S19. Amount of metallic Ni, Co, and Mn deposited on the Li metal anodes.

Fig. S20. Nyquist plots of Li||NCM811 cells with the a) ISP50 and b) PVDF binders. c) Equivalent circuit for Li||NCM811 cells.

Fig S21. Normalized concentrations of evolved gases from cells with different cathodes after the formation cycle, as measured by QMS.

Fig. S22. Cross-sectional SEM images of cycled NCM811 cathodes using the a) ISP50 and b) PVDF binders.

Fig. S23. dQ/dV curves of NCM811 cathodes using a) PVDF and b) ISP50 binders.

Fig. S24. Long-term cycling performance of NCM811 cathodes with a) PVDF and b) ISP50 binder at high temperature (55 °C).

Fig. S25. Cross-sectional SEM images of the ISP50 cathodes with different thickness (different areal mass loadings).

Fig. S26. Long-term cycling performance of the PVDF cathode with 31.1 mg cm^{-2}.

Fig S27. Extended cycling performance of the ISP50 cathodes with different areal mass loadings. b) Table shows the end of life (80% capacity retention) for different areal mass loading of ISP50 cathodes.

Fig S28. a) Galvanostatic charge-discharge profiles and b) cycling performance of the ISP50 cathodes with low-binder-content.

Fig. S29. Galvanostatic charge-discharge profiles of the double-stacked pouch-type full cell.

Fig S30. Cycling performance of the reassembled coin cell with recovered ISP50 cathode from the pouch cell after 60 cycles.

Table S1. Details on the calculation of the gravimetric energy densities (excluding packaging materials) of coin cells with ISP cathodes.

Table S2. Comparison of the electrochemical performance between the ISP cathode (this work) and previously reported cathodes containing various binders.

Table S3. Details on the calculation of the gravimetric and volumetric energy density of the double-stacked pouch-type full cell (including package materials). The area of the cathode and anode in the cell is 30 × 40 mm^2 and 32 × 42 mm^2, respectively.

Table S4. Comparison of the strategy, cathode-type, areal capacity, N/P ratio, energy density, and cycle performance of pouch-type full cell fabricated in this work and previously reported high-energy-density pouch-type full cells (Li-free denotes configurations where the anode initially contains no reserve Li).

Video S1. Qualitative analysis of self-healing in ISP50.

Video S2. Qualitative analysis of self-healing in ISP67.

Supplemental references

Note 1. The synthesis of the polymers.

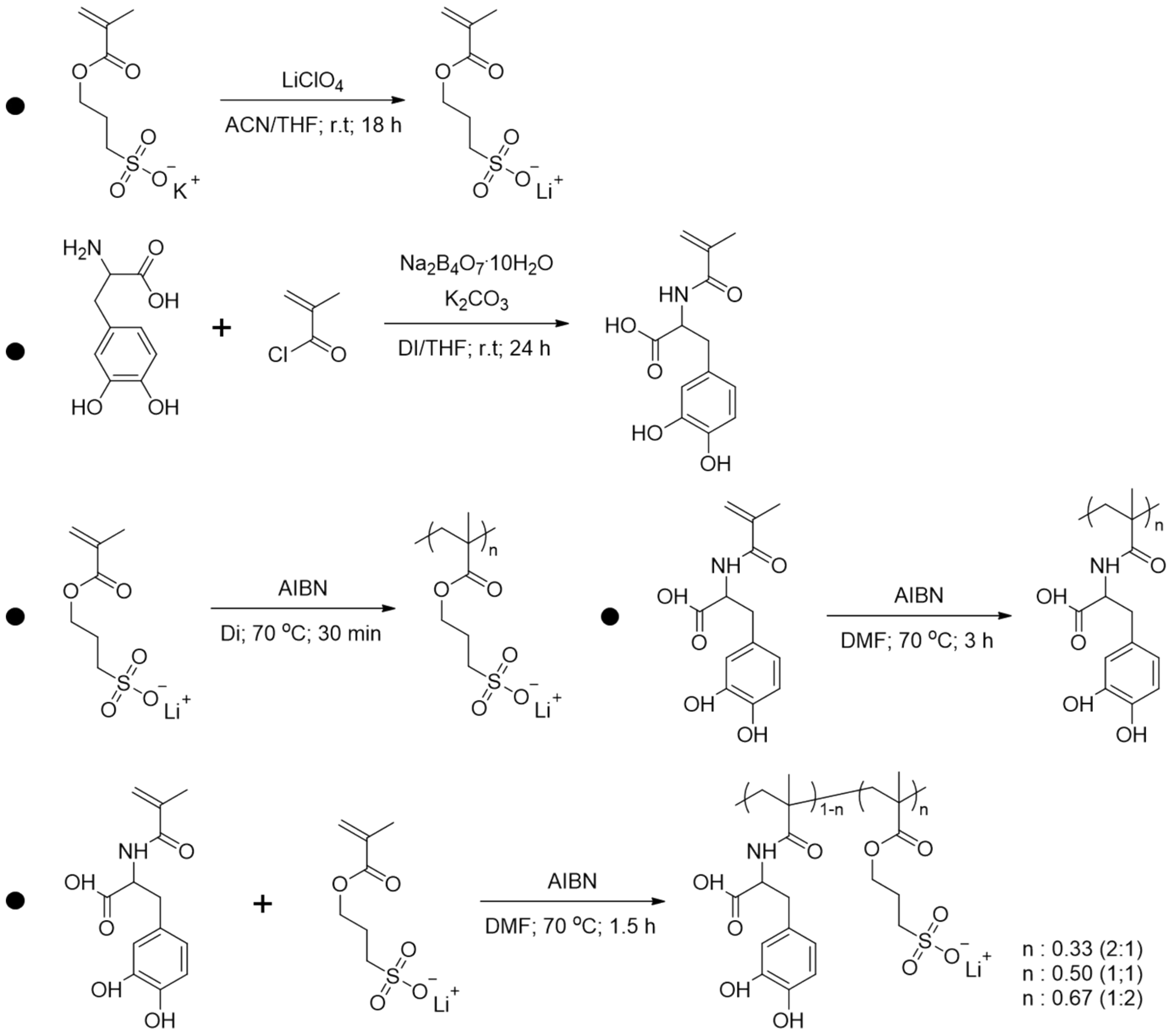

Synthesis scheme for Li[SPMA], DOPA, ISP0, ISP33, ISP50, ISP67, and ISP100 polymers

Materials.

3-Sulfopropyl methacrylate potassium salt, Lithium perchlorate, 2, 2'-azobis(isobutyronitrile), Sodium tetraborate decahydrate, Glycerol, and Methacryloyl chloride were purchased from Sigma-Aldrich. 3-(3,4-Dihydroxyphenyl)-L-alanine was purchased from the TCI. N-methylpyrrolidone (NMP) was purchased from Samchun Chemical. NCM811 was purchased from Posco Chemical, and Super P was purchased from Welcos. PVDF (KF1100, Mn = 168.8 kDa, polydispersity index = 2.94, KUREHA Chem. Ind.) was used as the reference polymeric binder in the cathode electrode.

Synthesis of 3-sulfopropyl methacrylate lithium salt (LSP).

3-Sulfopropyl methacrylate potassium salt (11.07 g, 45 mmol) and Lithium perchlorate (5.75 g, 54 mmol) were mixed in 100 mL tetrahydrofuran/acetonitrile co-solvent ((5/5), v/) for ion exchange (at room temperature, 12 h). The solution was centrifuged (5000 rpm, 5 min). After that, the solvent of the supernatant was removed by a rotary evaporator. The product was dried in a vacuum oven for 10^{-3} torr (over 24 h). The yield was 89.4% (8.62 g, 40 mmol). ^{1}H NMR (500 MHz, D2O, δ): 6.14 (s, -CH), 5.71 (s, -CH), 4.28 (t, J = 6.3, -CH2), 3.02 (t, J = 7.3, -CH2), 2.14 (m, J = 7.4, -CH2), 1.92 (s, -CH3). ^{7}Li NMR (500MHz, D2O, δ): 0.12 (s, -Li$^+$). ^{13}C NMR (500MHz, D2O, δ): 169.79, 135.92, 126, 63.76, 47.81, 23.72, 17.40.

Synthesis of methacryloyl 3,4-dihydroxyl-L-phenylalanine (DOPA).

Borate Anhydrous (29.58 g, 150 mmol) was added in 250 mL DI water for Ar fuzzing (1 h). After 1 h stirring, 3,4-dihydroxyl-L-phenylalanine (9.96 g, 50 mmol) and sodium carbonate (19 g, 180 mmol) were added to the reactor. After 30 min stirring, 4.8 mL methacryloyl chloride diluted by 15 mL tetrahydrofuran was dropwise for 15 min. The solution was stirred under Ar condition (24 h). 12 mL of Hydrochloric acid was injected and stirred for 1 h. After the stirring, the product was extracted in ethyl acetate two times with 0.1 M HCl aqueous and twice with brine. The organic phase was dried by anhydrous $MgSO_4$, concentrated up to 20 mL via rotary evaporation. The crude solution was precipitated in hexane. The white solid was dried in a vacuum oven for 10^{-3} torr (18 h). ^{1}H NMR (500 MHz, DMSO, δ): 8.72 (d, J = 2.9, -OH), 7.95 (d, J = 8.1, -NH), 6.61 (m, J = 5.1, -CH in aromatic), 6.48 (m, J = 2.0, -CH in aromatic), 5.63 (s, -CH2), 5.33 (t, J = 1.43, -CH2), 4.33 (m, J = 3.0, -CH), 2.91 (m, J = 4.6, -CH2), 2.80 (m, J = 3.9, -CH2), 1.80 (s, -CH3). ^{13}C NMR (500 MHz, DMSO, δ): 173.26, 167.47, 144.88, 143.72, 139.47, 128.75, 119.79, 119.54, 116.40, 115.26, 59.75, 35.73, 18.54.

Reactivity calculation of LSP and DOPA via the Mayo-Lewis equation.

To calculate the reactivity ratio (r_x) between LSP and DOPA, test polymerization was carried out at feed batch ratios of 50:50 mol% and 75:25 mol% (LSP:DOPA). After that, the r_x between monomers (LSP and DOPA) was calculated from the Mayo-Lewis Equation. (N1):

$$F_1 = 1 - F_2 = \frac{r_1 f_1^2 + f_1 f_2}{r_1 f_1^2 + 2 f_1 f_2 + r_2 f_2^2} \tag{N1}$$

where F_x and f_x are the mole fraction of monomer x in the copolymer and in the feed batch, respectively. The feed batch ratio of monomers for polymerization was determined by the r_x calculated through the Equation. N1 (r_{DOPA} : 0.617 and r_{LSP} : 1.682).

Synthesis of the series of ISPs.

3-sulfopropyl methacrylate lithium salt (LSP), meth acryloyl 3,4-dihydroxyl-L-phenylalanine (DOPA), and 2,2'-Azobis(2-methyl propionitrile) were mixed in 5 mL N N-Dimethylformamide for polymerization (Di water in ISP100) (at 70 °C, 3 h). The crude solution was precipitated in tetrahydrofuran twice. The product was dried in a vacuum oven for 10^{-3} torr (over 24 h). ISP0: ^{1}H NMR (500 MHz, DMSO, δ): 9.03-8.31 (Br, -OH), 6.85-6.31 (Br, -CH in aromatic), 4.50-4.01 (Br, -CH), 3.16-2.47 (Br, -CH2, -CH2), 1.52-0.23 (Br, -CH3). ISP33: ^{1}H NMR (500 MHz, DMSO, δ): 9.00-8.43 (Br, -OH), 6.95-6.23 (Br, -CH in aromatic), 4.56-3.94 (Br, -CH, -CH2), 3.44-3.26 (Br, -CH2), 3.16-1.88 (Br, -CH2, CH2), 1.51-0.04 (Br, -

CH3). ISP50: ^{1}H NMR (500 MHz, DMSO, δ): 9.07-8.46 (Br, -OH), 6.93-6.29 (Br, -CH in aromatic), 4.46-3.73 (Br, -CH, -CH2), 3.44-3.26 (Br, -CH2), 3.16-1.88 (Br, -CH2, CH2), 1.51-0.04 (Br, -CH3). ISP67: ^{1}H NMR (500 MHz, DMSO, δ): 8.91-8.50 (Br, -OH), 6.84-6.31 (Br, -CH in aromatic), 4.61-3.68 (Br, -CH, -CH2), 3.44-3.26 (Br, -CH2), 3.16-1.88 (Br, -CH2, CH2), 1.51-0.02 (Br, -CH3). ISP100: ^{1}H NMR (500 MHz, D2O, δ): 4.30-3.84 (Br, -CH2), 3.01-2.91 (Br, -CH2), 2.18-1.49 (Br, -CH2, -CH2), 1.29-0.71 (Br, -CH3).

Preparation of the polymer gels.

The polymers (1 g) were dissolved in the 10 wt% glycerol solution (10 g) (1 g glycerol/9 g EtOH). The solution was drop cast on the Teflon mold. After that, the solution dried at 30 °C over 24 h.

Characterization of the polymers.

^{1}H, ^{7}Li, and ^{13}C NMR spectroscopy were measured on an Avance III HD500 instrument using deuterium oxide and dimethyl sulfoxide-d$_6$. Number average (M_n) and weight-average (M_w) molecular weights were obtained by gel permeation chromatography (GPC) with a SHIMADZU LC solution, with DMF as the eluent, by comparison with a calibration curve of polystyrene (PS) standards. The electrochemical properties of the polymer gels were measured using electrochemical impedance spectroscopy (EIS; IM6, Zahner). The resistance of the polymer gels was determined by the high-frequency region with consistent impedance in the Bode plot with polymer gel with electrolyte (5 μm) in sandwiched devices of FTO glass. The ionic conductivity (σ) of the polymer gels was calculated as following Equation. (N2):

$$\sigma = \frac{1}{\rho} = \frac{l}{RA} \tag{N2}$$

where ρ, R, l, and A are the resistivity, resistance, thickness, and cross-sectional area of the polymer gels. The rheological properties were obtained using an MCR-92, Anton Paar Rheometer with an 8 mm parallel plate on an oscillation basis. Differential scanning calorimetric (DSC) measurements were performed using a Perkin-Elmer Pyris DSC 4000 instrument under an N_2 atmosphere at a heating and cooling rate of 10 °C min^{-1}. A tensile test was performed using ESM303, Mark-10 with the specimen of cylindrical shape with a diameter of 2 mm and length of 2 cm (tensile speed of 100 mm min^{-1}). The optical microscopy images were obtained using an optical microscope (ZEISS Axioplan microscope). Fourier transform infrared spectroscopy (FT-IR) analysis was conducted using the Spectrum Two, PerkinElmer. Transition metal ion concentrations in liquid electrolytes were quantified using inductively coupled plasma mass spectroscopy (ICP-MS, Thermo ICAP 6000, Thermo Scientific). Transmission electron microscopy (TEM, JEM-2100F, JEOL) operated at 200 kV was utilized to examine the structural configuration of binder-coated NCM811 particles. Scanning electron microscopy (SEM, S-4800, Hitachi) and 3D laser confocal microscopy (VK-X3050, KEYENCE) were employed to evaluate the uniform dispersion of electrode components. Adhesion strength measurements were conducted using a Surface and Interfacial Characterization Analysis System (SAICAS, SAICAS EN-EX, Daipla Wintes). Interfacial component analysis of cycled NCM811 electrodes was performed using time-of-flight secondary ion mass spectrometry (TOF-SIMS, TOF-SIMS 5, ION TOF) and X-ray photoelectron spectroscopy (XPS, Scientific K-Alpha system, Thermo Scientific). Synchrotron-based X-ray nano-computed tomography (nano-CT) images were acquired at the 7C X-ray Nano Imaging (XNI) beamline at PLS-II. The field of view and pixel size were set to 76 μm and 44 nm, respectively. Each 3D tomography image was reconstructed from 900 projection images collected with 0.4 s exposure time using the filtered back-projection algorithm in Octopus software (TESCAN). Transmission electron microscopy (TEM) samples were prepared using a focused ion beam (FIB, Helios 5 CX, Thermo Fisher). Post-mortem structural examinations of NCM811 electrodes were conducted via scanning transmission electron microscopy coupled with electron energy loss spectroscopy (STEM-EELS, JEM ARM 200F, JEOL). The microstructure of thick electrodes was examined using SEM and an ion milling system (IM4000, Hitachi High-Technologies).

Electrochemical measurements

NCM811 cathodes were fabricated via a slurry coating method, where NCM811 particles, super P (carbon black), and the polymeric binder were mixed homogeneously at a mass ratio of 90:5:5. For low-binder-content electrodes, the ratios were adjusted to 96:2:2 (2 wt% binder) and 97:2:1 (1 wt% binder). The resulting slurry was cast onto aluminum foil to prepare electrodes with mass loading of 22.1 mg cm^{-2}, and additional samples were prepared with higher mass loadings of 31.0 mg cm^{-2}, 40.9 mg cm^{-2}, 51.5 mg cm^{-2}, 63.4 mg cm^{-2}, and 86.1 mg cm^{-2}. The electrodes were dried under vacuum at 70 °C for at least 12 h, then cut into disks and assembled into CR2032 coin cells (Welcos) in an argon-filled glove box. Each cell consisted of a Celgard 2400 separator, lithium metal counter electrodes (300 μm for half cell and 100 μm for full cell), and a liquid electrolyte. The electrolyte used was 1.0 M $LiPF_6$ dissolved in a mixture of ethylene carbonate (EC), ethyl methyl carbonate (EMC), and dimethyl carbonate (DMC) (3:5:2 v/v/v), with the addition of 5 wt% Fluoroethylene carbonate (FEC) as an additive. Galvanostatic Cycling tests were performed at 25 °C on a battery cycler (WBCS 3000, Wonatech) within a voltage range of 2.7–4.3 V. A CCCV protocol was applied: during charging, the constant voltage step at 4.3 V was held until the current dropped below 0.05 C before proceeding to discharge. The formation cycle was conducted at 0.05 C, followed by subsequent cycling at rates ranging from 0.1 C to 3 C. The calculation details of the coin cell were described in Table S1. Ex-situ electrochemical impedance spectroscopy (EIS) measurements were conducted using a VSP-300 (BioLogic) with an amplitude of 10 mV over a frequency range of 100 kHz to 0.1 Hz. A double-stacked pouch-type full cell was fabricated, incorporating thick ISP cathodes (3.0 cm × 4.0 cm) paired with a thin Li metal anode (40 μm, 3.2 cm × 4.2 cm, 40 μm, N/P ratio of 0.69) and an E/C ratio of 2.5 g Ah^{-1}. The mass loading of the NCM811 cathode for the pouch cell was 52.3 mg cm^{-2}. The energy density of the pouch cell was calculated from the entire pouch cell, including both active and inactive components (including package materials). Calculation details for gravimetric/volumetric energy densities of the pouch cell were described in Table S3.

Galvanostatic intermittent titration technique (GITT)

GITT measurements were performed by applying a current pulse of 0.1 A g^{-1} for 5 min, followed by a resting phase of 30 min. The closed-circuit voltage (CCV) and quasi-open-circuit-voltage (QOCV) were obtained from the GITT measurements. The internal cell resistance at various lithiation/delithiation states was calculated using the following Equation. (N3):

$$Internal\,resistance(\Omega) = \frac{|CCV - QOCV|}{|I_{applied}|} \tag{N3}$$

The lithium-ion diffusion coefficient (D_{Li^+}) was calculated using the Weppner-Huggins equation, derived from the square root of time dependence of the potential change ($t \ll L^2 D^{-1}$, where L is the film thickness) (Equation. (N4)):

$$D_{Li^+} = \frac{4}{\pi\Delta\tau}(\frac{m_B V_M}{M_B S})^2(\frac{\Delta E_s}{\Delta E_\tau})^2 \tag{N4}$$

Here, $\Delta\tau$ is the duration of the applied pulse, m_B is the mass of NCM811 in the electrode, V_M is the molar volume of NCM811 (20.33 cm^3 mol^{-1}), M_B is the molar mass of NCM811 (97.28 g mol^{-1}), S is the area of the electrode, ΔE_s is the total voltage change overall steps, and ΔE_τ is the voltage change during the pulse step.

In-situ galvanostatic electrochemical impedance spectroscopy (GEIS) measurements

In-situ GEIS measurements were conducted under a constant current of 0.5 C during both lithiation and delithiation phases. Impedance spectra were collected every 10 minutes using a VSP-300 (BioLogic). The setup employed two independent channels: one for recording impedance spectra and the other for monitoring voltage profiles. A sinusoidal current with a 10 mA amplitude was applied over a frequency range from 100 kHz to 0.01 Hz.

Gas evolution analysis

Quantitative analysis of evolved gases was performed using a quadrupole mass spectrometer (el Inc.), in conjunction with a custom gas-tight syringe equipped with a gas valve. Pouch-type full cells incorporating different binders were subjected to a formation cycle (2.7–4.3 V at 50 °C) to assess binder-dependent gas evolution. After cycling, the evolved gas was extracted and analyzed by monitoring the ion currents of target gases relative to total pressure, under constant composition conditions. Calibration was performed using standard gases (H_2, 99.999%; CH_2, 10.697% in N_2; O_2, 20.8% in air; Ar, 99.999%; and CO_2, 99.999%).

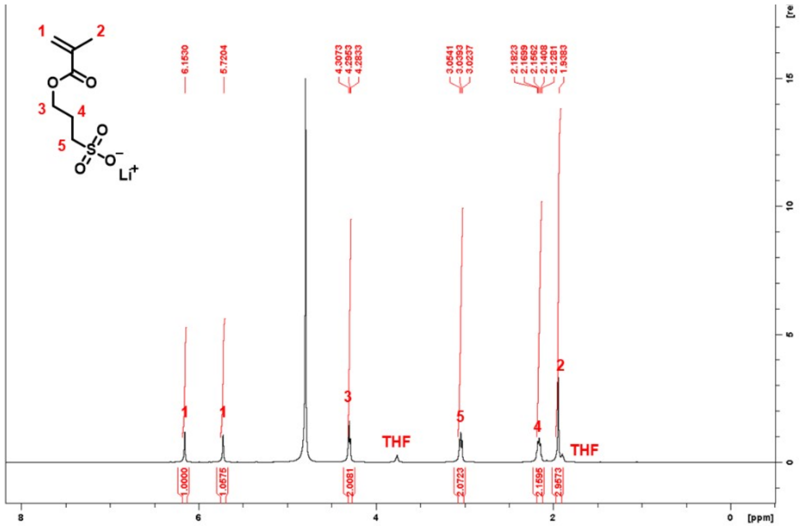

^{1}H NMR spectroscopy of lithium sulfopropyl methacrylate (LSP).

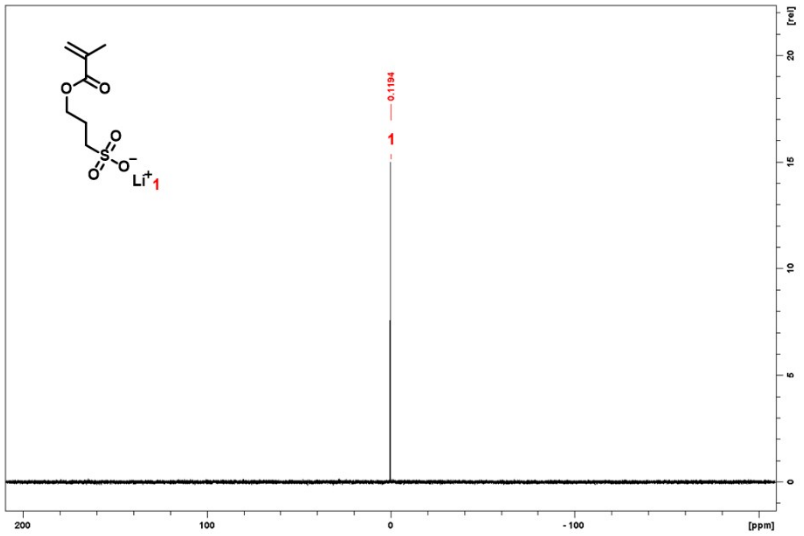

^{7}Li NMR spectroscopy of lithium sulfopropyl methacrylate (LSP).

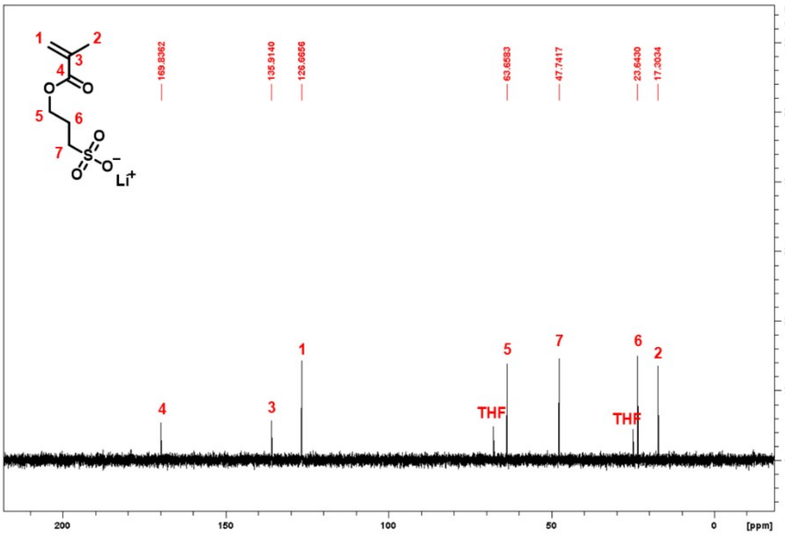

^{13}C NMR spectroscopy of lithium sulfopropyl methacrylate (LSP).

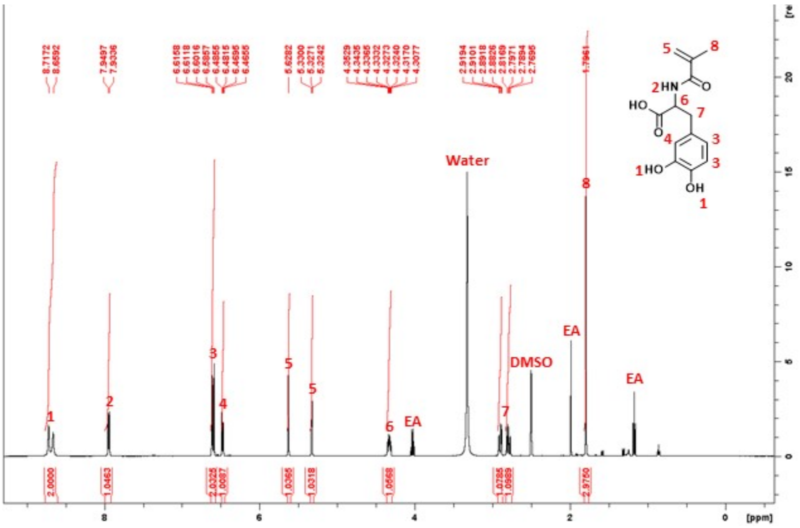

^{1}H NMR spectroscopy of methacryloyl 3,4-dihydroxyl-L-phenylalanine (DOPA).

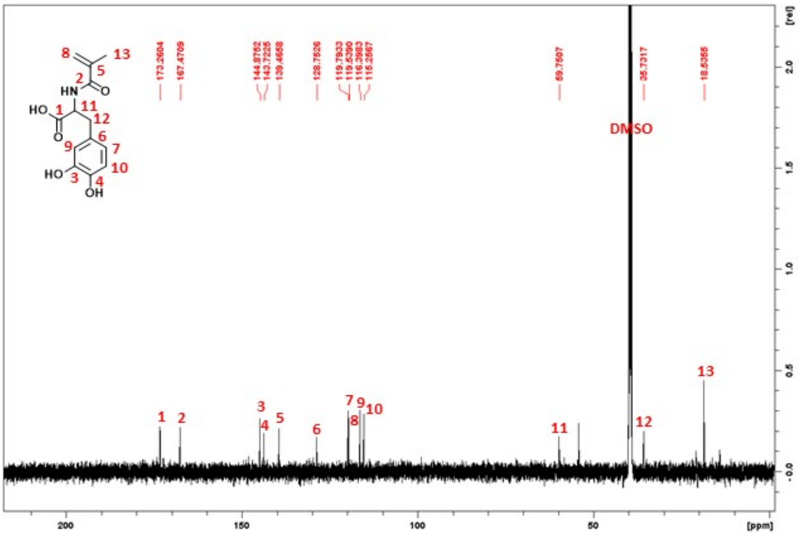

^{13}C NMR spectroscopy of methacryloyl 3,4-dihydroxyl-L-phenylalanine (DOPA).

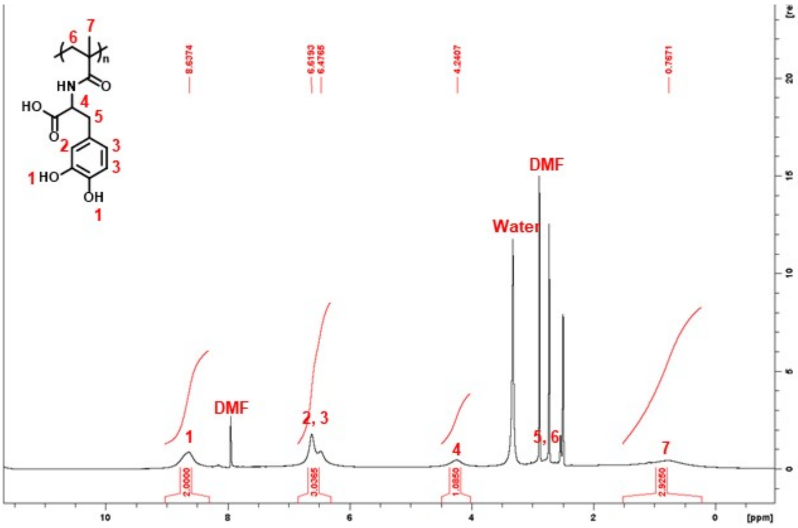

^{1}H NMR spectroscopy of ISP0.

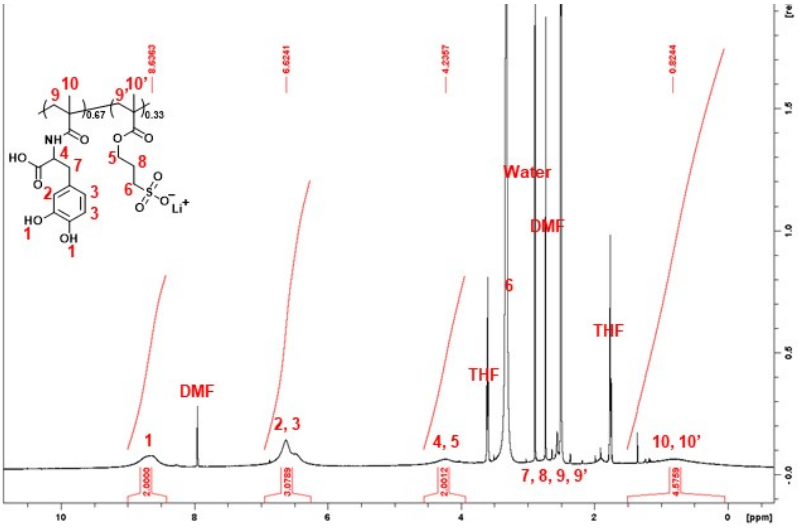

^{1}H NMR spectroscopy of ISP33.

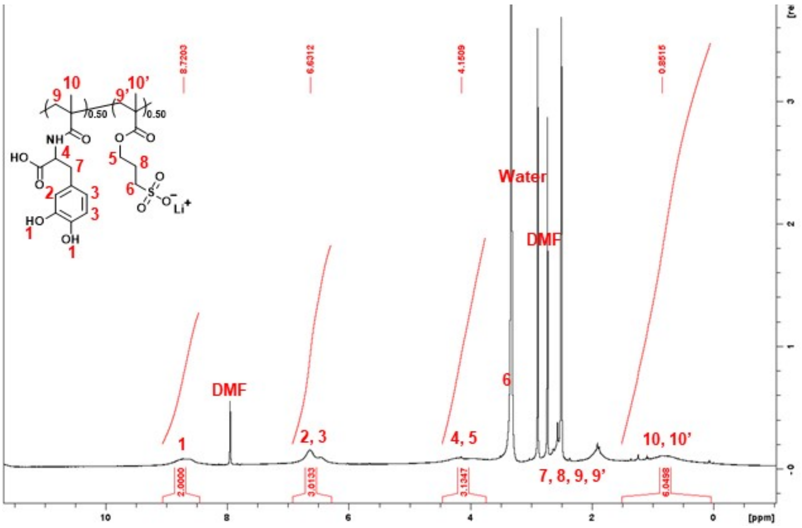

^{1}H NMR spectroscopy of ISP50.

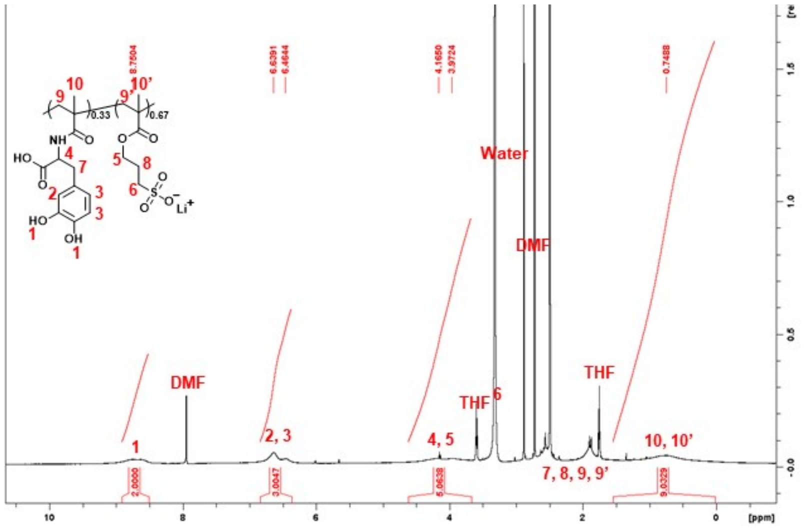

^{1}H NMR spectroscopy of ISP67.

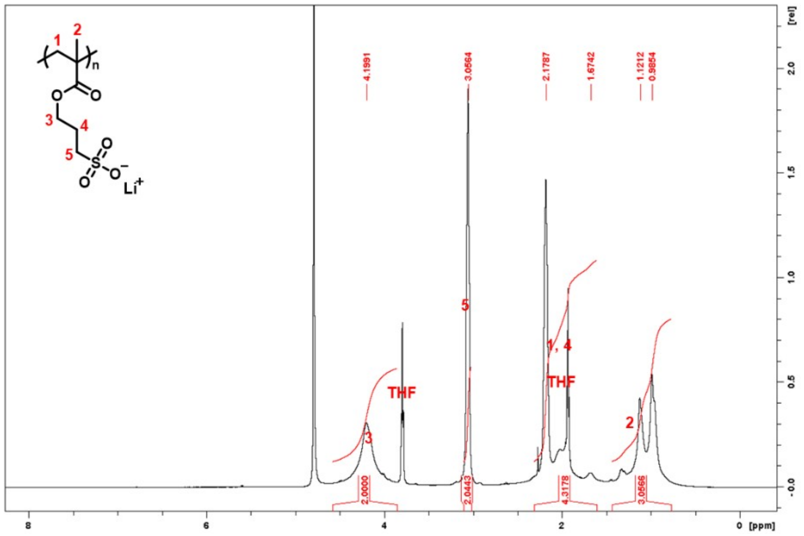

^{1}H NMR spectroscopy of ISP100.

Fig. S1. ^{1}H NMR, ^{7}Li NMR, and ^{13}C NMR spectra of lithium sulfopropyl-methacrylate (LSP), ^{1}H NMR and ^{13}C NMR spectroscopy of methacryloyl 3,4-dihydroxyl-L-phenylalanine (DOPA), and ^{1}H NMR spectra of ISP0, ISP33, ISP50, ISP67, and ISP100.

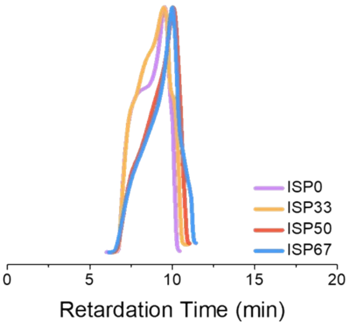

	M_n	PDI
ISP0	602 k	1.48
ISP33	553 k	1.55
ISP50	403 k	1.65
ISP67	367 k	1.77

Fig. S2. GPC profiles in the ISP series.

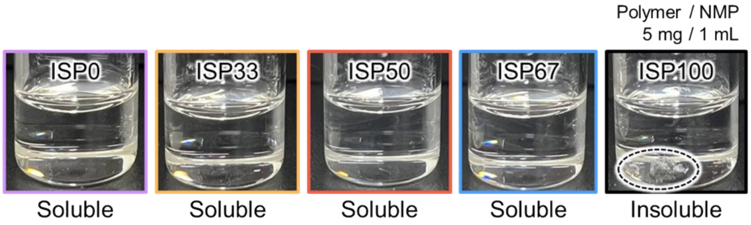

Fig. S3. Solubility of the ISP series in NMP.

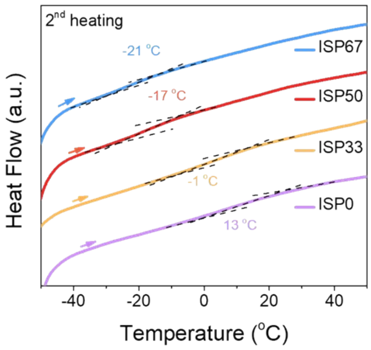

Fig. S4. Temperature-dependent behavior in the ISP series by DSC.

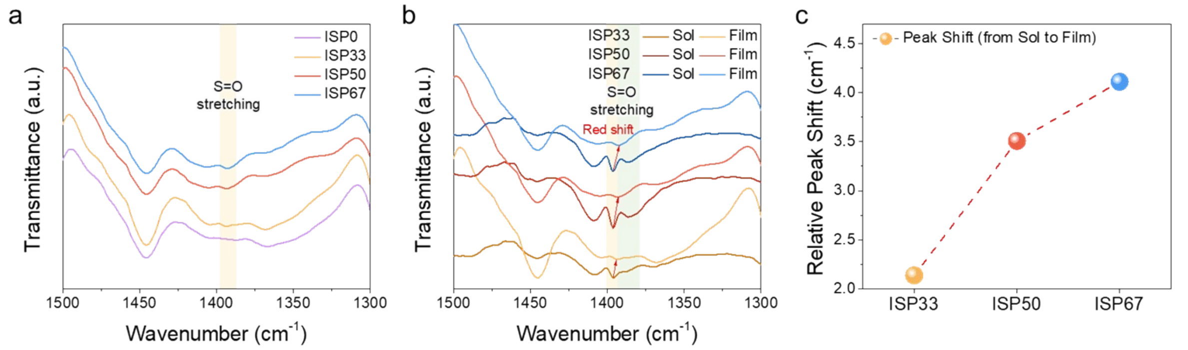

Fig. S5. The FT-IR spectra of a) the ISP series in the film state, and b) comparison of ISP33, ISP50, and ISP67 in solution and film state. c) Relative peak shift between solution and film state in ISP33, ISP50, and ISP67.

The ionic moieties (sulfonate anion) on the side chain of ISP facilitate interaction with other ionic moieties, which was confirmed by Fourier transform infrared spectroscopy (FT-IR) analysis.[S1] In ISP0 (film) without ionic moieties, the S=O stretching peak at 1394 cm^{-1} was not observed, while ISPs with ionic moieties revealed the S=O peak at 1396 cm^{-1} (in solution) and 1391~1393 cm^{-1} (in film) (**Fig. S5a** and **S5b**). The ISP33, ISP50, and ISP67 films showed a red shift compared with the solution state, indicating an increased interaction with sulfonate anions. Especially, ISPs with more ion moieties exhibited a more prominent red shift (**Fig. S5c**). The electrostatic interaction between these ion moieties forms ion-cluster.[S2-S4]

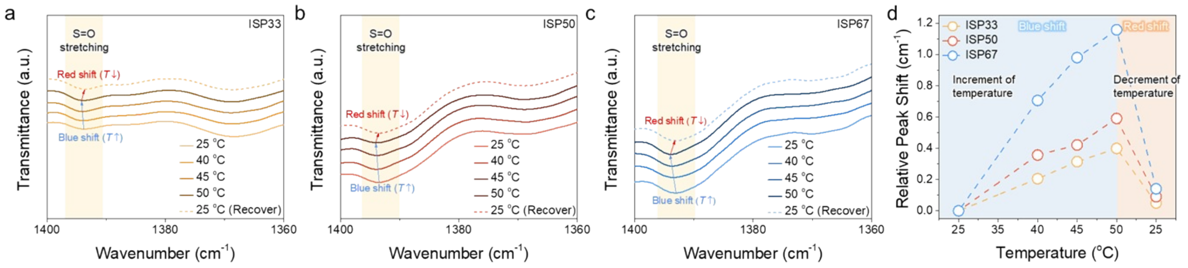

Fig. S6. a-c) The FT-IR spectra and d) relative peak shift of the ISP33, ISP50, and ISP67 films depending on the temperature.

The shift of the S=O peak with temperature was observed. The S=O peak of the ISP33, ISP50, and ISP67 films exhibited a blue shift at increased temperatures, and then a red shift after returning to 25 °C (**Fig. S6**). This shift implies that the interaction between ion moieties decreases with increased temperature and subsequently increases when temperature decreases. These investigations demonstrate that the formation of ion-cluster is reversible.

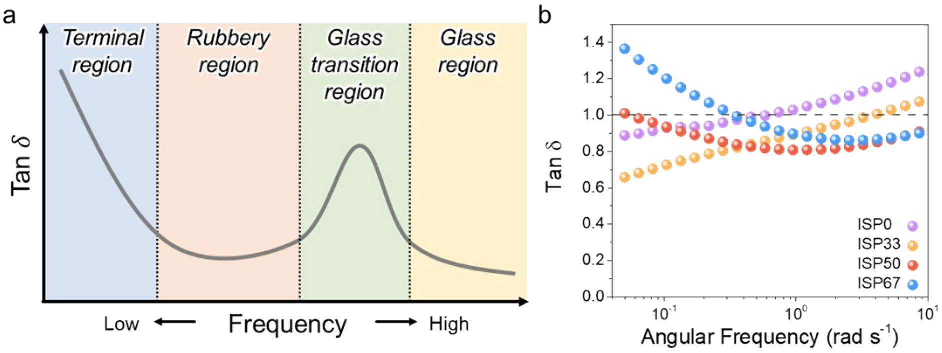

Fig. S7. a) Diagram of the polymer chain behavior (Tan δ) depending on the frequencies.[S5] b) The tan δ of the ISP series under angular frequencies.

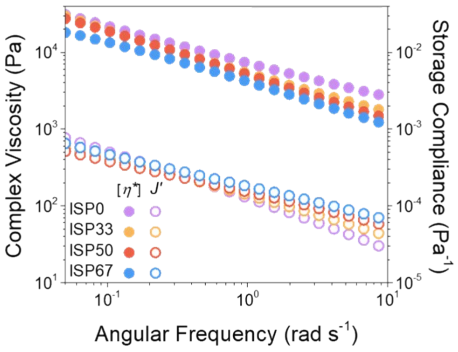

Fig. S8. The complex viscosity and storage compliance of the ISP series under angular frequencies.

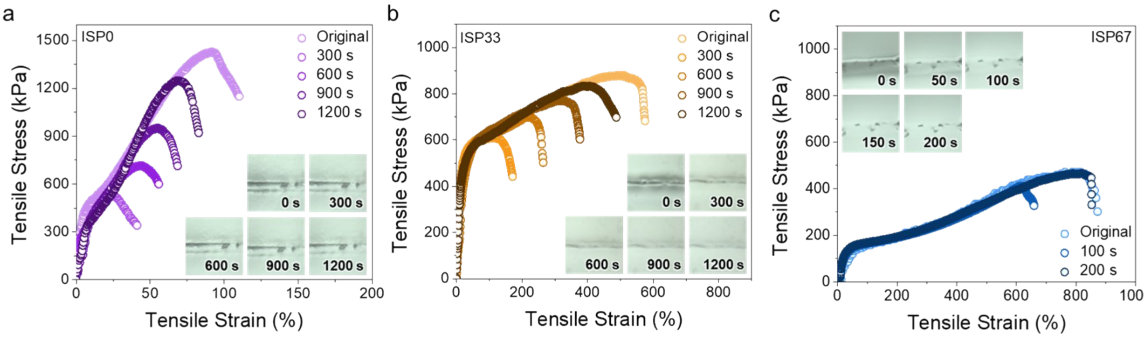

Fig. S9. The tensile S-S curve depending on the time (quantitative self-healing), along with inset OM images (qualitative self-healing) of the a) ISP0, b) ISP33, and c) ISP67.

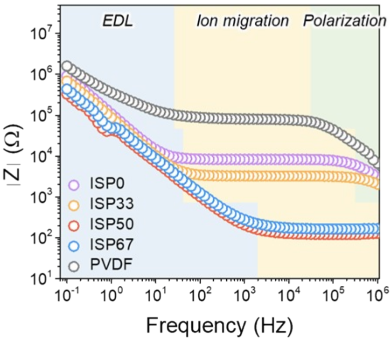

Fig. S10. Bode plots of the ISP series and PVDF depending on the polarization, ion migration, and electrical double layer (EDL) regions.

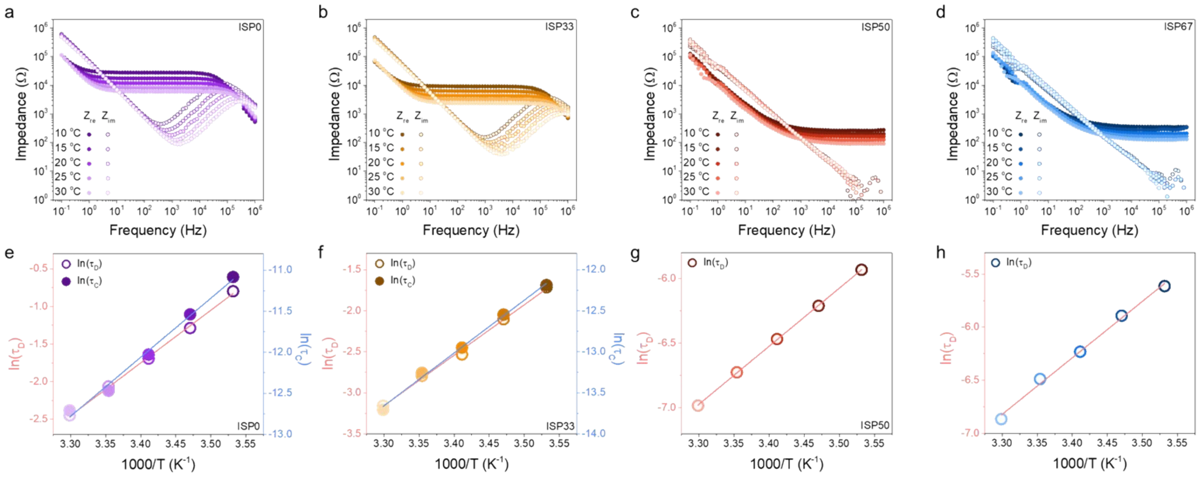

Fig. S11. a-d) Real and imaginary impedance depending on the frequencies, and e-h) relaxation time of the ISP series at the various temperatures.

In materials with high ionic conductivity (ISP50 and ISP67 in this study), mobile ions exhibit ion migration behavior even at high frequency, with no observed polarization region (**Fig. S10** and **S11a-d**). Thus, it is required to investigate the real & imaginary impedances at extremely high frequencies to confirm the polarization region; however, the real & imaginary impedances become unstable above 10^6 Hz, leading to low reliability. Therefore, lowering the ionic conductivity is required to confirm the polarization region (~ 10^6 Hz).[S6, S7] Herein, lowering the measurement temperature (at -40 °C) decreased ionic conductivity, and confirmed the behavior of mobile ions in the polarization region and charge relaxation frequency (**Fig. 2c**).

The τ_C^{-1} and τ_D^{-1} are expressed as following Equation. (N5) and (N6)[S8]

$$\tau_C^{-1} = R_B^{-1}C_B^{-1} = R_B^{-1}\frac{d}{\varepsilon A} = \rho^{-1}\varepsilon^{-1} \tag{N5}$$

$$\tau_D^{-1} = R_B^{-1} C_{EDL}^{-1} = R_B^{-1} \frac{d'}{\varepsilon A'} = \rho'^{-1} \varepsilon^{-1} \quad \text{(in EDL)} \qquad \text{(N6)}$$

where R_B, C_B, C_{EDL}, ε, d, A, and ρ are bulk resistance, bulk capacitance, constant phase element from EDL, permittivity, distance, area, and resistivity, respectively. Therefore, the relaxation frequencies (time) are determined by ρ and ε, which exhibit temperature dependence according to the Arrhenius equation.[S9, S10] Consequently, $\ln(\tau_C)$ and $\ln(\tau_D)$ have linear correlations with temperature (**Fig. S11e-h**).[S6, S8]

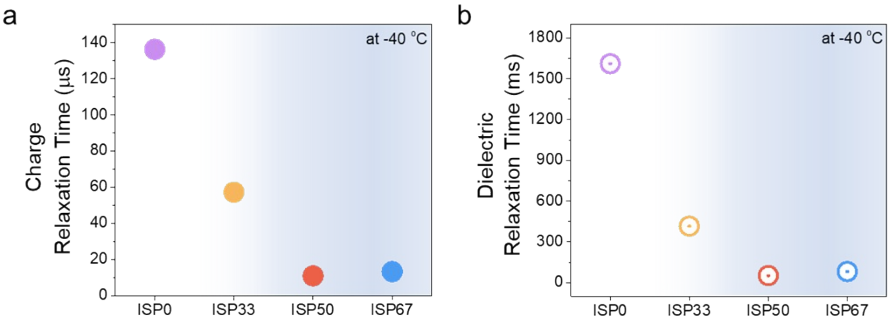

Fig. S12. a) Charge and b) dielectric relaxation time of mobile ions in the ISP series at -40 °C.

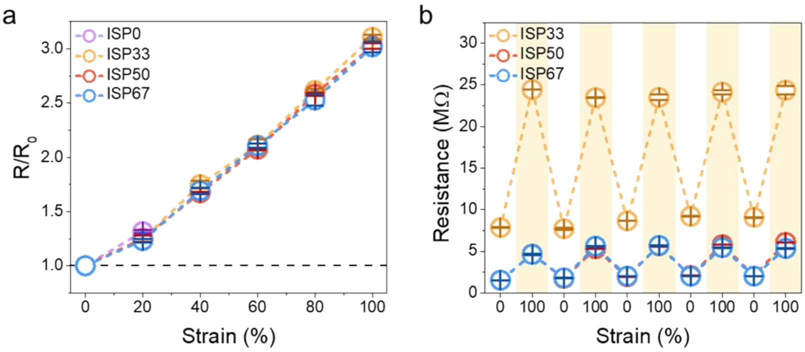

Fig. S13. Resistance change of the ISP series a) under several stretching conditions and b) under repeated 100% stretching condition.

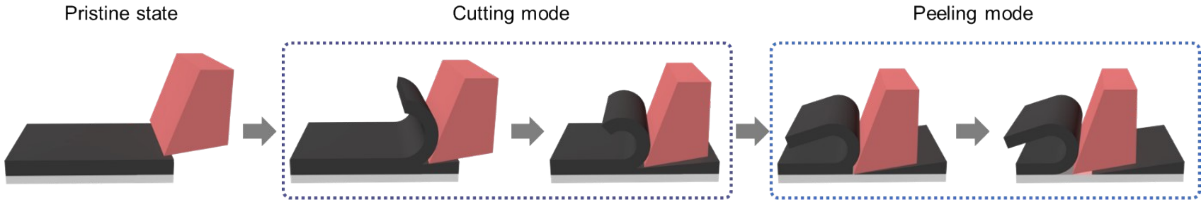

Fig. S14. Schematic illustration of the SAICAS process.

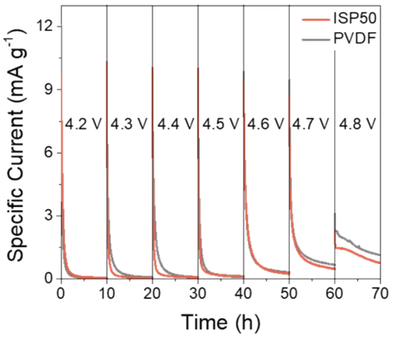

Fig. S15. Electrochemical floating analysis of the NCM811 cathodes.

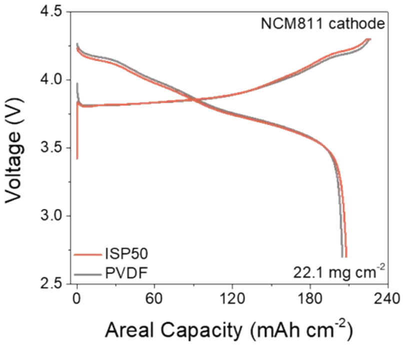

Fig. S16. Galvanostatic charge-discharge profiles of the ISP50 and PVDF cathodes.

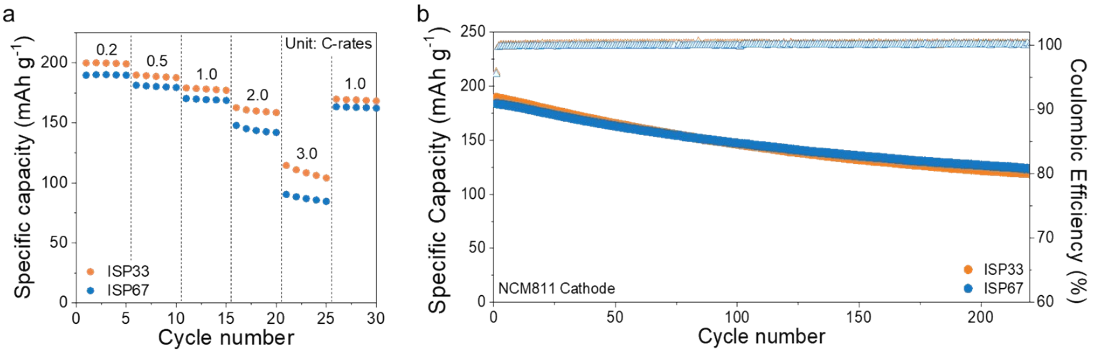

Fig S17. a) Discharge rate capability and b) long-term cycling performance of NCM811 cathodes with different ISP binders.

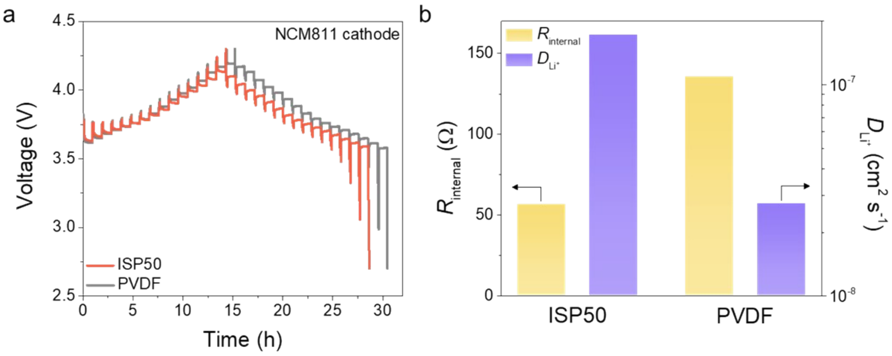

Fig. S18. a) GITT profiles obtained upon the repeated current stimuli at 0.5 C. b) Average internal resistance and Li⁺ diffusion coefficient values of cathodes.

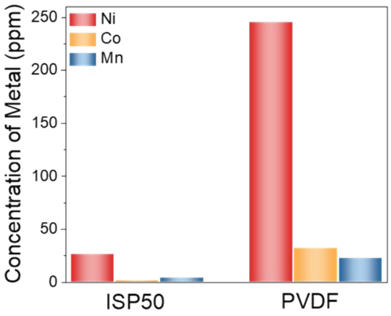

Fig. S19. Amount of metallic Ni, Co, and Mn deposited on the Li metal anodes.

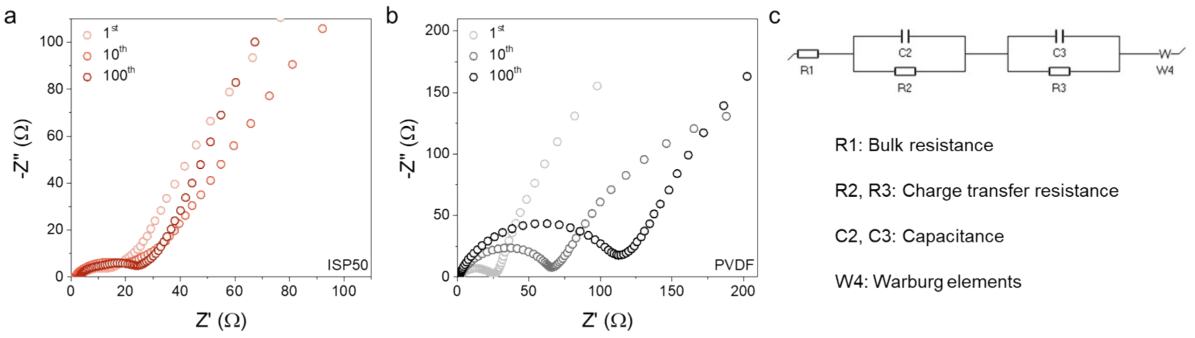

Fig. S20. Nyquist plots of Li||NCM811 cells with the a) ISP50 and b) PVDF binders. c) Equivalent circuit for Li||NCM811 cells.

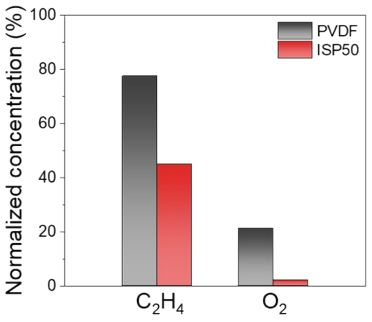

Fig S21. Normalized concentrations of evolved gases from cells with different cathodes after the formation cycle, as measured by QMS.

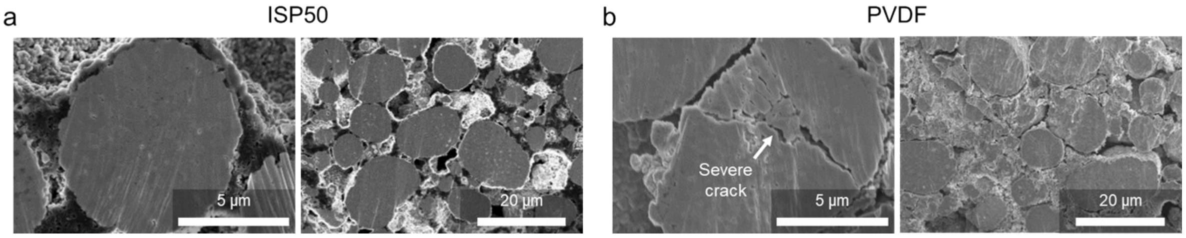

Fig. S22. Cross-sectional SEM images of cycled NCM811 cathodes using the a) ISP50 and b) PVDF binders.

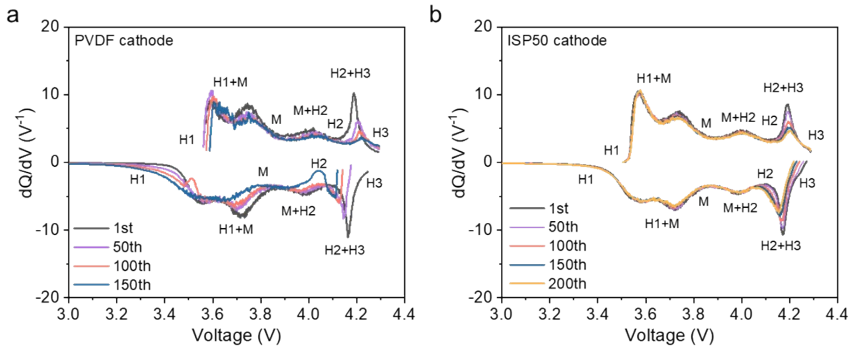

Fig S23. dQ/dV curves of NCM811 cathodes using a) PVDF and b) ISP50 binders.

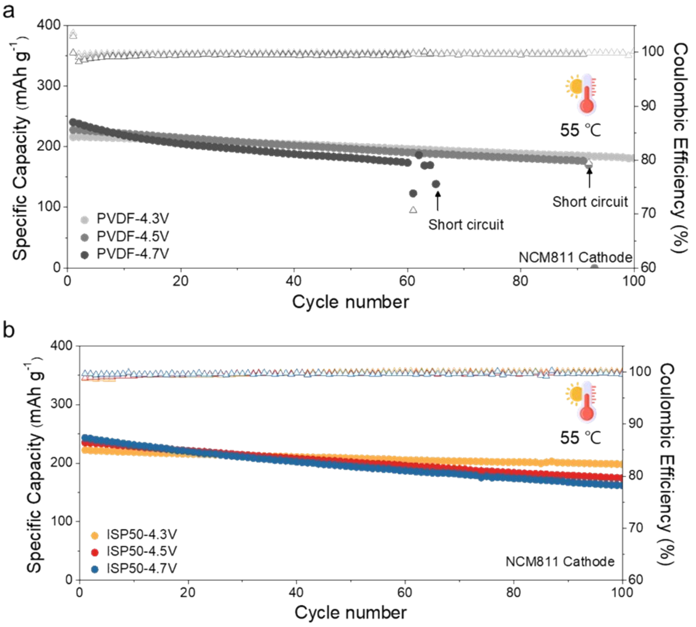

Fig. S24. Long-term cycling performance of NCM811 cathodes with (a) PVDF and (b) ISP50 binder at high temperature (55 °C).

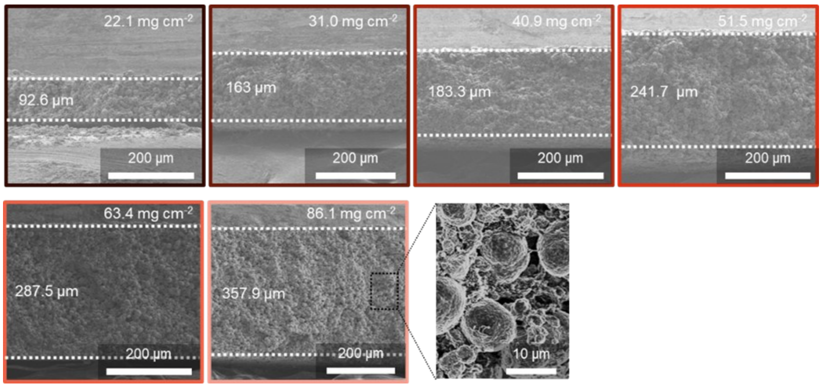

Fig. S25. Cross-sectional SEM images of the ISP50 cathodes with different thickness (different areal mass loadings).

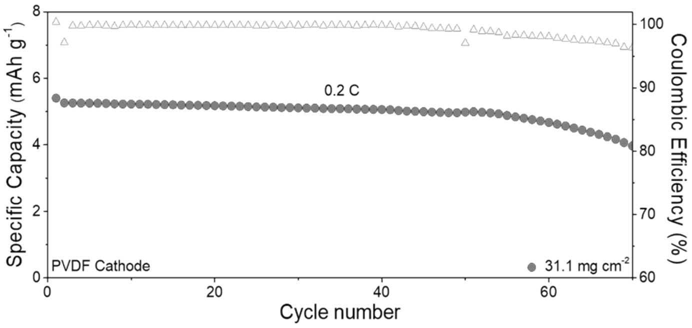

Fig. S26. Long-term cycling performance of the PVDF cathode with 31.1 mg cm^{-2}.

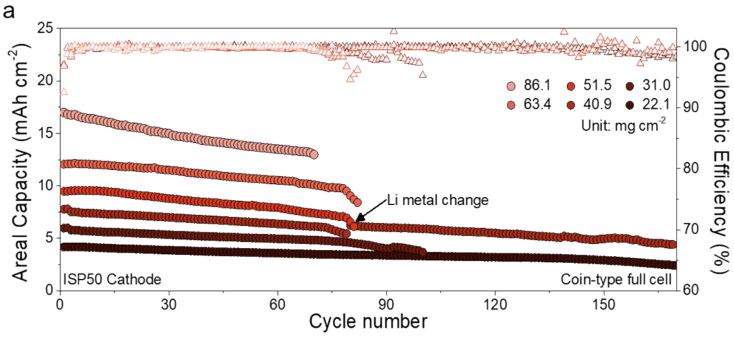

b

Areal mass loading of cathode (mg cm^{-2})	Cycle at 80% retention
22.1	129th
31.0	81th
40.9	73th
51.5	69th
63.4	79th
86.1	60th

Fig S27. Extended cycling performance of the ISP50 cathodes with different areal mass loadings. b) Table shows the end of life (80% capacity retention) for different areal mass loading of ISP50 cathodes.

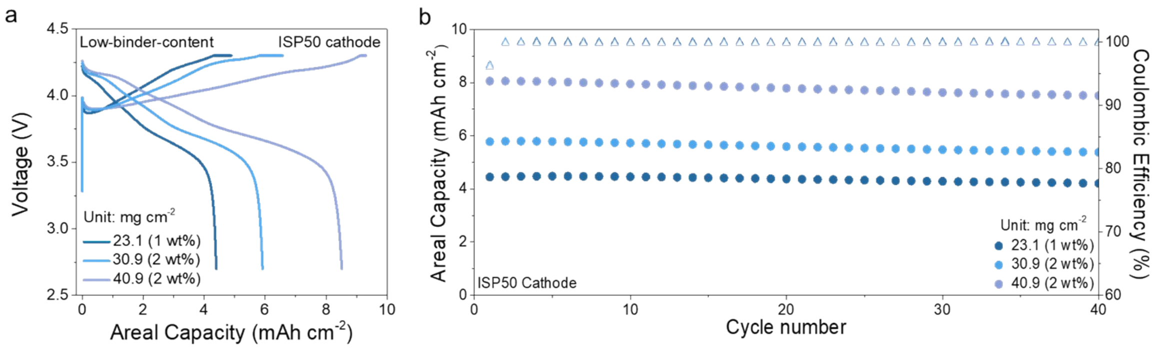

Fig S28. a) Galvanostatic charge-discharge profiles and b) cycling performance of the ISP50 cathodes with low-binder-content.

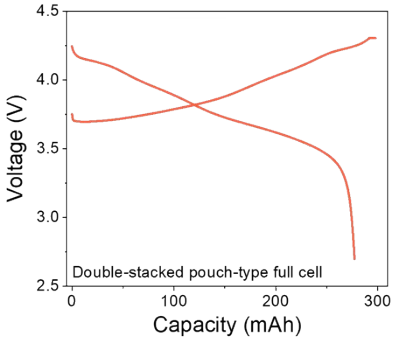

Fig. S29. Galvanostatic charge-discharge profiles of the double-stacked pouch-type full cell.

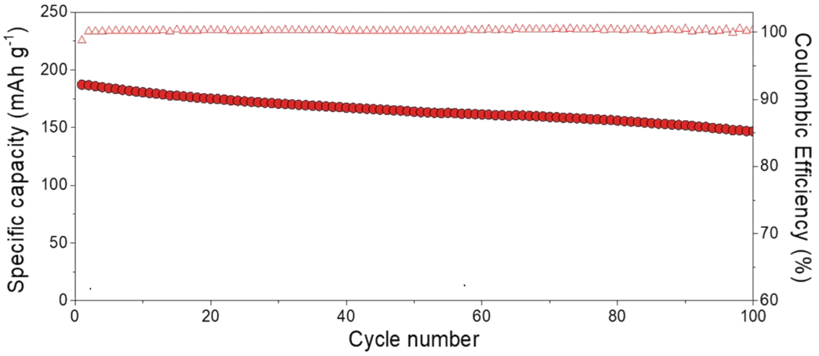

Fig S30. Cycling performance of the reassembled coin cell with recovered ISP50 cathode from the pouch cell after 60 cycles.

Table S1. Details on the calculation of the gravimetric energy densities (excluding packaging materials) of coin cells with ISP cathodes.

$$Gravimetric\ energy\ density\ \left(Wh\ kg^{-1}\right) = \frac{Capacity\ (Ah) \times Workingvoltage\ (V)}{Total\ mass\ of\ the\ cell\ (kg)}$$

Cell type	Cathode (g)	Anode (g)	Electrolyte (g)	Separator (g)	Total mass (g)	Capacity (mAh)	Working voltage (V)	Gravimetric energy density (Wh kg^{-1})
ISP #1	20.41	8.22	8.44	3.07	40.13	3.38	3.80	319.61
ISP #2	27.40	8.22	11.97	3.07	50.65	4.79	3.80	359.24
ISP #3	35.17	8.22	15.50	3.07	61.96	6.20	3.80	380.36
ISP#4	43.49	8.22	20.21	3.07	74.98	8.09	3.80	409.73
ISP #5	52.83	8.22	25.32	3.07	89.43	10.13	3.80	430.28
ISP#6	70.65	8.22	35.13	3.07	117.06	14.05	3.80	456.12
PVDF #1	22.61	8.22	8.81	3.07	42.70	3.52	3.80	313.64
PVDF #2	27.47	8.22	10.77	3.07	49.53	4.31	3.80	330.62
PVDF #3	32.34	8.22	10.85	3.07	54.48	4.34	3.80	302.79

Table S2. Comparison of the electrochemical performance between the ISP cathode (this work) and previously reported cathodes containing various binders.

Materials	Cathode type	Areal mass loading (mg cm^{-2})	Areal capacity (mAh cm^{-2})	Reference
ISP binder	NCM811	86.1	17.9	This work
Bottlebrush polymer	NCM811	27	5.2	S11
Sol-binder	NCM811	32	5.2	S12
PNCI binder	NCM811	21.7	4.5	S13
P(CN-CF)$_{1/9}$ binder	LCO	26.0	4.5	S14
Chaperone binder	NCM811	60.0	8.0	S15
Poly(imide-siloxane) binder	NCM523	6.0	1.2	S16
Organosilicon-type binder	LCO	8.0	1.4	S17
Carrageenan binder	LNMO	10.0	1.3	S18
PR-co-PAA binder	NCM622	5.5	1.1	S19
Dextran sulfate lithium binder	LCO	3.0	0.63	S20
DSS-*co*-PAA lithium binder	NCM811	32.3	6.1	S21
Siloxane nanohybrid binder	NCM811	12.0	2.1	S22

Table S3. Details on the calculation of the gravimetric and volumetric energy density of the double-stacked pouch-type full cell (including package materials). The area of the cathode and anode in the cell is 30 × 40 mm^2 and 32 × 42 mm^2, respectively.

$$Gravimetric\ energy\ density\ \left(Wh\ kg_{cell}{}^{-1}\right) = \frac{Capacity\ (Ah) \times Working\ voltage\ (V)}{Total\ weight\ of\ pouch\ cell\ (kg)}$$

Anode current collector (g)	Cathode current collector (g)	Li metal anode (g)	Cathode (g)	Separator (g)	Electrolyte (g)	Al pouch (g)	Total weight (g)	Capacity (Ah)	Working voltage (V)	Gravimetric energy density (Wh kg^{-1})
0.0213	0.0847	0.0574	1.310	0.0342	0.693	0.576	2.777	0.277	3.82	381.1

$$Volumetric\ energy\ density\ \left(Wh\ L_{cell}{}^{-1}\right) = \frac{Capacity\ (Ah) \times Workingvoltage\ (V)}{Total\ volume\ of\ pouch\ cell\ (L)}$$

Anode current collector (μm)	Cathode current collector (μm)	Li metal anode (μm)	Cathode (μm)	Separator (μm)	Al pouch (μm)	Total thickness (μm)	Capacity (Ah)	Working voltage (V)	Volumetric energy density (Wh L^{-1})
10	20	80	508	48	160	826	0.277	3.82	1067.5

Table S4. Comparison of the strategy, cathode-type, areal capacity, N/P ratio, energy density, and cycle performance of pouch-type full cell fabricated in this work and previously reported high-energy-density pouch-type full cells (Li-free denotes configurations where the anode initially contains no reserve Li).

Strategy	Cathode type	Areal capacity for single-layer cathode (mAh cm^{-2})	N/P ratio	Gravimetric energy density (Wh kg^{-1})	Volumetric energy density (Wh L^{-1})	Cycle performance	Reference
Binder design	NCM811	11.6	0.69	381.1	1067.5	92.9%@60th cycle	This work
Advanced Electrolyte	NCM811	4.0	Li-free	325	-	80%@70th cycle	S23
Cathode coating	NCM811	4.85	Li-free	320	850	80%@300th cycle	S24
Binder design	NCM811	178.0	1.1	376	1043	82%@100th cycle	S25
Electrode architecture	NCM811	12.1	1.6	321	772	-	S26
Pressure control	NCM622	3.8	2.6	300	-	83%@200th cycle	S27
Artificial SEI	NCM523	4.4	1.5	340	-	83%@150th cycle	S28

Artificial SEI	NCM811	4.0	5.0	260	-	-	S29
Electrode architecture	NCM811	5	1.0	344	951	80%@50th cycle	S30
Pressure control	NCM622	3.5	3.0	350	-	80%@282th cycle	S31
Advanced Electrolyte	NCM811	3.02	2.5	323	-	92.9%@150th cycle	S32
Advanced Electrolyte	NCM811	3.8	2	360	-	74.0%@100th cycle	S33

Video S1. Qualitative analysis of self-healing in ISP50.

Video S2. Qualitative analysis of self-healing in ISP67.

Supplemental references

1. T. Agarwal, A. K. Prasad, S. G. Advani, S. K. Babu, and R. L. Borup, *J. Mater. Chem. A*, 2024, **12**, 14229.
2. S. Jang, S. Y. Kim, H. Y. Jung, and M. J. Park, *Macromolecules*, 2018, **51**, 3, 1120.
3. M. J. Park, *Mol. Syst. Des. Eng.*, 2019, **4**, 239.
4. Y. M. Kim, J. H. Kwon, S. Kim, U. H. Choi, and H. C. Moon, *Nat. Commun.*, 2022, **13**, 3769.
5. S. Kim, J. H. Kwon, Y. Bae, J. Kim, T. Park, and H. C. Moon, *Energy Environ. Sci.*, 2024, **17**, 8102.
6. I. You, D. G. Mackanic, N. Matsuhisa, J. Kang, J. Kwon, L. Beker, J. Mun, W. Suh, T. Y. Kim, J. B.-H. Tok, Z. Bao, and U. Jeong, *Science*, 2020, **370**, 961.
7. D. H. Ho, Y. M. Kim, U. J. Kim, K. S. Yu, J. H. Kwon, H. C. Moon, and J. H. Cho, *Adv. Energy Mater.*, 2023, **13**, 2301133.
8. H. W. Kim, E. Kim, J. Oh, H. Lee, and U. Jeong, *Adv. Sci.*, 2022, **9**, 2200687.
9. K. M. Diederichsen, H. G. Buss, and B. D. McCloskey, *Macromolecules*, 2017, **50**, 10, 3831.
10. K. Nakamura, T. Saiwaki, and K. Fukao, *Macromolecules*, 2010, **43**, 14, 6092.
11. N.-Y. Kim, J. Moon, M.-H. Ryou, S.-H. Kim, J.-H. Kim, J.-M. Kim, J. Band, and S.-Y. Lee, *Adv. Energy Mater.*, 2022, **12**, 2102109.
12. Y. He, L. Jing, L. Feng, S. Yang, J. Yang, X. Fu, W. Yang, and Y. Wang, *Adv. Energy Mater.*, 2023, **13**, 2203272.
13. D. Jeong, D.-S. Kwon, H. J. Kim, and J. Shim, *Adv. Energy Mater.*, 2023, **13**, 2302845.
14. L. Deng, J.-K. Liu, Z. Wang, J.-X. Lin, Y.-X. Liu, G.-Y. Bai, K.-G. Zheng, Y. Zhou, S.-G. Sun, and J.-T. Li, *Adv. Energy Mater.*, 2024, **14**, 2401514.
15. L. Jing, Y. Ji, L. Feng, X. Fu, X. He, Y. He, Z. Zhu, X. Sun, Z. Liu, M. Yang, W. Yang, and Y. Wang, *Energy Storage Mater.*, 2022, **45**, 828.
16. Y. Wang, N. Dong, B. Liu, G. Tian, S. Qi, and D. Wu, *Energy Storage Mater.*, 2023, **56**, 621.
17. J. Ahn, H.-G. Im, Y. Lee, D. Lee, H. Jang, Y. Oh, K. Chung, T. Park, M.-K. Um, J. W. Yi, J. Kim, D. J. Kang, and J.-K. Yoo, *Energy Storage Mater.*, 2022, **49**, 58.
18. B. Chang, D. H. Yun, I. Hwang, J. K. Seo, J. Kang, G. Noh, S. Choi, and J. W. Choi, *Adv. Mater.*, 2023, **35**, 2303787.
19. H. Yang, R.-M. Gao, X.-D. Zhang, J.-Y. Liang, X.-H. Meng, Z.-Y. Lu, F.-F. Cao, and H. Ye, *Adv. Mater.*, 2022, **34**, 2204835.
20. H. Huang, Z. Li, S. Gu, J. Bian, Y. Li, J. Chen, K. Liao, Q. Gan, Y. Wang, S. Wu, Z. Wang, W. Luo, R. Hao, Z. Wang, G. Wang, and Z. Lu, *Adv. Energy Mater.*, 2021, **11**, 2101864.
21. Q. Gan, N. Qin, H. Guo, F. Zhang, H. Yuan, W. Luo, Z. Li, Y. Li, L. Lu, Z. Xu, L. Wang, J. Lu, and Z. Lu, *ACS Energy Lett.*, 2024, **9**, 4, 1562.
22. J. Jang, J. Ahn, J. Ahn, U. Jeong, J. Yoon, J. K. Park, W. Shin, M. J. Kang, M.-K. Cho, D. J. Kang, J. Kim, J.-K. Yoo, and H.-G. Im, *Adv. Funct. Mater.*, 2024, **34**, 2410866.
23. Z. Yu, H. Wang, X. Kong, W. Huang, Y. Tsao, D. G. Mackanic, K. Wang, X. Wang, W. Huang, S. Choudhury, Y. Zheng, C. V. Amanchukwu, S. T. Hung, Y. Ma, E. G. Lomeli, J. Qin, Y. Cui, and Z. Bao, *Nat. Energy*, 2020, **5**, 526.

24. Y. Qiao, H. J. Yang, Z. Chang, H. Deng, X. Li, and H. S. Zhou, *Nat. Energy*, 2021, **6**, 653.

25. J.-H. Kim, K. M. Lee, J. W. Kim, S. H. Kweon, H.-S. Moon, T. Yim, S. K. Kwak, and S.-Y. Lee, *Nat. Commun.*, 2023, **14**, 5721.

26. J.-H. Kim, J.-M. Kim, S.-K. Cho, N.-Y. Kim, and S.-Y. Lee, *Nat. Commun.*, 2022, **13**, 2541.

27. C. J. Niu, H. Lee, S. R. Chen, Q. Y. Li, J. Du, W. Xu, J. G. Zhang, M. S. Whittingham, J. Xiao, and J. Liu, *Nat. Energy*, 2019, **4**, 551.

28. X. Q. Zhang, T. Li, B. Q. Li, R. Zhang, P. Shi, C. Yan, J. Q. Huang, and Q. Zhang, *Angew. Chem. Int. Ed.*, 2020, **59**, 3252.

29. M. S. Kim, J. H. Ryu, Deepika, Y. R. Lim, I. W. Nah, K. R. Lee, L. A. Archer, and W. I. Cho, *Nat. Energy*, 2018, **3**, 889.

30. D.-Y. Han, S. Kim, S. Nam, G. Lee, H. Bae, J. H. Kim, N.-S. Choi, G. Song, and S. Park, *Adv. Sci.*, 2024, **11**, 2402156.

31. D. Liu, B. Wu, Y. Xu, J. Ellis, A. Baranovskiy, D. Lu, J. Lochala, C. Anderson, K. Baar, D. Qu, J. Yang, D. Galvez-Aranda, K-J. Lopez, P. B. Balbuena, J. M. Seminario, J. Liu, and J. Xiao, *Nat. Energy*, 2024, **9**, 559.

32. G. Lu, X. Wu, M. Huang, M. Zhang, Z. Piao, X. Zhong, C. Li, Y. Song, C. Chang, K. Yu, and G. Zhou, *Energy Environ. Sci.*, 2024, **17**, 9555.

33. J. Kim, D. G. Lee, J. H. Lee, S. Kim, C.-Y. Park, J. Lee, H. Kwon, H. Cho, J. Lee, D. Son, H.-T. Kim, N.-S. Choi, T. K. Lee, and J. Lee, *Energy Environ. Sci.*, 2025.